J. Fluid Mech. (2008), *vol.* 608, *pp.* 1–20.
doi:10.1017/S0022112008001845 Printed in the United Kingdom

Wave absorbing system using inclined perforated plates

I. H. CHO[1] AND M. H. KIM[2]

[1]Department of Marine Industrial Engineering, Cheju National University, Jeju 690-756, Korea

[2]Department of Civil Engineering, Texas A&M University, College Station, TX 77843, USA

(Received 1 November 2007 and in revised form 20 March 2008)

The interaction of oblique monochromatic incident waves with horizontal/inclined/dual porous plates is investigated in the context of two-dimensional linear potential theory and Darcy's law (the normal velocity of fluid passing through a thin porous plate is linearly proportional to the pressure difference across it). The developed theory is verified by both small-scale and full-scale experiments. First, matched eigenfunction expansion (MEE) solutions for a horizontal porous plate are obtained. The relationship between the plate porosity and the porous parameter is obtained from systematic model tests by using six porous plates with different sizes and spacing of circular holes. Secondly, a multi-domain boundary-element method (BEM) using simple-sources (second-kind modified Bessel function) is developed to confirm the MEE solutions and to apply to more general cases including inclined or multiple porous plates. The BEM-based inner solutions are matched to the eigenfunction-based outer solutions to satisfy the outgoing radiation condition in the far field. Both analytical and BEM solutions with the developed empirical porous parameter agree with each other and correlate well with both small-scale data from a two-dimensional wave-tank test and full-scale measurement in a large wave basin. Using the developed predictive tools, wave-absorption efficiency is assessed for various combinations of porosity, water depth, submergence depth, wave heading, and plate/wave characteristics. In particular, it is found that the performance can be improved by imposing the proper inclination angle near the free surface. The optimal porosity is near porosity $P = 0.1$ and the optimal inclination angle is around 10° as long as the plate length is greater than 20 % of the wavelength. Based on the selected optimal parameters (porosity $= 0.1$ and inclination angle $= 11.3^\circ$), the effective wave-absorption system for MOERI's square basin is designed.

1. Introduction

Wave absorbers are installed in wave tanks and harbour walls to minimize wave reflection. For a wave tank experiment, wave reflection must be minimized from the endwall to simulate the open-sea condition and avoid wave distortion at the measuring section. Effective wave absorbers are also important in suppressing remnant waves inside wave basins after the wave generators are stopped.

A variety of structures, shapes, and materials are used for wave absorption in wave tanks. Ouellet & Datta (1986) conducted a review study for various wave absorbers installed at 48 worldwide wave basins. Most of the passive wave absorbers are classified into vertical and inclined types. The vertical wave absorber is commonly constructed of multiple rows of porous vertical metal sheets with the porosity

progressively decreased toward the end. This kind of wave absorber is widely operated in deep-water wave basins. On the other hand, the inclined wave absorber is made up of beach with constant or varying slopes, for which various materials, such as gravel/stone, transversal bars, wire screen and horse hair, are used. Its slope has to be mild, usually less than 1:10, to obtain a good dissipation of wave energy, which requires a long distance for wave absorption. Particularly in deep-water tanks, it will use up a large portion of the valuable tank space. In order to minimize the absorption space, different ideas and arrangements including the addition of roughness or porosity on their surfaces have been experimented with.

Vertical porous plates are widely used for wave absorption in deep-water tanks. To achieve desirable efficiency, they typically use properly spaced multiple porous sheets with a progressive decrease in porosity toward the end. The incident wave is partly transmitted and partly trapped/reflected across the porous plates generating partial standing waves between respective plates and the rear wall. The number and the spacing of the plates as well as the porosity of each plate are important design parameters for maximizing wave absorber efficiency.

During the past few decades, there have been many theoretical and experimental studies regarding the wave-absorption performance by vertical porous plates. For example, the wave transmission of a thin vertical porous plate placed in deep water was investigated by Tuck (1975). He discussed the application of Darcy's law for flows across porous plates and suggested that in the case of sinusoidal oscillations the velocity across the material with fine pores can be related to the pressure drop by a complex-valued frequency-dependent parameter, which accounts for both viscous and inertial effects. Along the same lines, Chwang (1983) developed a porous wavemaker theory and found that the porous effect reduces the wave amplitude as well as the hydrodynamic force on the wavemaker. Evans (1990) analysed the wave reflection by a number of thin porous plates fixed in a narrow wave tanks and showed that the reflected wave energy is largely reduced if the front porosity is greater than the rear porosity. Twu & Lin (1991) developed a highly effective wave-absorption system consisting of a finite number of thin porous plates based on Darcy's law, in which experimental tests were carried out and the results agreed well with the theoretical solutions.

One of the major problems associated with using multiple vertical porous plates is that it also demands a large space to achieve desirable efficiency. Another problem is large force by trapped waves and possible wave generation by the thin plates undergoing hydroelastic motions. In view of this, horizontal porous plates may be an alternative candidate for wave absorption. The formulation of the interaction of submerged horizontal porous plates with waves is in general more complicated than that of vertical porous plates. Siew & Hurley (1977) and McIver (1985), for instance, studied the diffraction of linear waves by a submerged rigid flat plate. They showed that it can reflect a significant amount of incident wave energy in a certain wave-frequency region. Possible applications of submerged horizontal plates for offshore wave control have been reviewed by Yu & Chwang (2002) and Cho & Kim (1999). Cho & Kim (1998) studied the performance of a tensioned horizontal flexible membrane as a wave barrier and their experimental results agreed reasonably with their numerical predictions. Chwang & Wu (1994) showed that submerged horizontal plates with moderate geometric porosity can dissipate wave energy effectively. Wu, Wan & Fang (1998) investigated wave reflection from a vertical wall with a submerged horizontal porous plate attached to it and found that the plate with proper porosity can significantly reduce not only the wave run-up

but also the reflection coefficient. The efficiency of horizontal porous plates as wave absorber is strongly dependent on the plate length, the submergence depth, and the porous parameter. Yip & Chwang (2000) investigated the hydrodynamic performance of a perforated vertical wall breakwater with an internal horizontal plate and found that the horizontally submerged porous plate inside the chamber can enhance the performance and structural stability.

In § 2, the matched eigenfunction expansion (MEE) solutions of wave reflection from a vertical wall with a horizontal submerged porous plate attached to it are investigated by using the eigenfunction expansion method. The fluid domain is divided into upper and lower regions divided by the horizontal porous plate, and the analytic velocity potentials are obtained in the respective regions after applying Darcy's law at the porous plate. The porous parameter plays an important role in wave-absorption efficiency and the wave load on the plate. The porous parameter is empirically determined from a least-squares fitting with the experimentally measured data. In § 3, a multi-domain boundary-element method (BEM) is independently developed first to confirm the MEE solutions and secondly to apply to the cases of inclined/dual porous plates. The present analytic and BEM solutions can be used for any incident angles and are extensively verified by a series of small-scale and full-scale experimental results, as summarized in §§ 4 and 5.

The small-scale experiments were conducted with various types of submerged porous plates (horizontal, inclined, dual) in a two-dimensional wave tank at the Maritime and Ocean Engineering Research Institute (MOERI). From the experiments, the porous-parameter formula (relationship between plate porosity P and porous parameter b) was obtained. Using the empirical formula, the small-scale experimental results for various wave conditions and plate porosities correlated well with the analytical and BEM solutions developed here. Encouraged by the agreement between the numerical prediction and the small-scale-test data, the performance of a prototype inclined wave absorber in front of MOERI's square-basin wall is subsequently tested for various wave conditions, wave headings, and plate inclination angles. The full-scale data also correlate well with the numerical predictions. Based on the results from both theoretical and experimental investigations, the final design of the new, efficient MOERI wave absorber, which consists of multiple inclined horizontal porous plates in front of several vertical porous plates, was completed.

2. Matched-eigenfunction-expansion analytic method

We consider the interaction of a horizontal porous plate with monochromatic oblique incident waves. Cartesian axes are chosen with the x-axis along the mean free surface and the y-axis pointing vertically upwards. The water depth is denoted by h, and the length and the submergence depth of the porous plate by a and d, respectively. The porous plate is installed horizontally in front of a vertical wall. It is also assumed that the fluid is incompressible and inviscid. The viscous effects are to be included through Darcy's law, i.e. the perforated plate is thin and made of arrays of fine holes so that the normal velocity of the fluid passing through the porous plate is linearly proportional to the pressure difference between the two sides of the plate (Chwang 1983; Chwang & Wu 1994). With the above assumptions, linear potential theory can be applied. The fluid particle velocity can then be described by the gradient of a velocity potential $\Phi(x, y, z, t)$. Assuming harmonic motion of frequency ω, the velocity potential can be written as $\Phi(x, y, z, t) = \mathrm{Re}[\phi(x, y)\mathrm{e}^{\mathrm{i}k_z z - \mathrm{i}\omega t}]$, where $k_z = k_1 \sin\theta$ is the z-component wavenumber and θ is the heading of incident waves

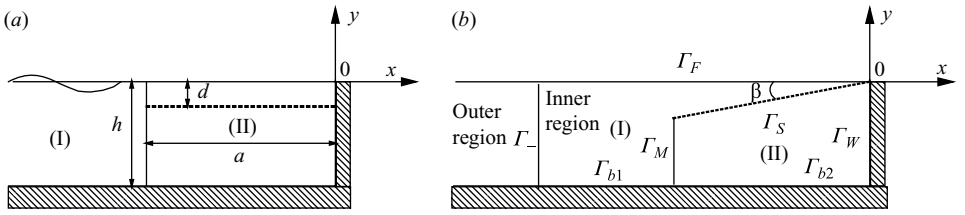

FIGURE 1. (*a*) Definition sketch of a submerged horizontal porous plate with a vertical wall. (*b*) Integration domains for a numerical solutions.

with respect to the x-axis. The velocity potential ϕ satisfies the modified Helmholz equation

$$\frac{\partial^2\phi}{\partial x^2} + \frac{\partial^2\phi}{\partial y^2} - k_1^2 \sin^2\theta\phi = 0 \quad \text{in the fluid,} \tag{2.1}$$

with the following boundary conditions

$$\frac{\partial\phi}{\partial y} - \nu\phi = 0 \quad \text{on} \quad y = 0 \left(\nu = \frac{\omega^2}{g}\right), \tag{2.2}$$

$$\frac{\partial\phi}{\partial y} = 0 \quad \text{on} \quad y = -h, \tag{2.3}$$

$$\frac{\partial\phi^+}{\partial y} = \frac{\partial\phi^-}{\partial y} = \mathrm{i}\sigma(\phi^- - \phi^+) \quad \text{on} \quad y = -d, -a < x < 0, \tag{2.4}$$

$$\frac{\partial\phi}{\partial x} = 0 \quad \text{on} \quad x = 0, \tag{2.5}$$

$$\lim_{x\to-\infty}\left[\frac{\partial(\phi - \phi_I)}{\partial x} + \mathrm{i}k_1\cos\theta(\phi - \phi_I)\right] = 0, \tag{2.6}$$

where g is the acceleration due to gravity and k_1 is the wavenumber. The radiation condition (2.6) is applied to diffraction potential $(\phi - \phi_I)$, where ϕ_I is the incident wave potential. Superscript $\pm$(equation (2.4)) means $-d \pm 0$. According to Mei (1974), the imaginary part of σ is related to the inertia effect and it can be neglected when the plate is thin and the holes are not large. The imaginary part of σ is proportional to flow accelerations, and thus has nothing to do with energy dissipation. The positive real value of σ represents viscous effects and can be obtained directly from experiment. The positive real value of σ is called the porous-effect parameter $(= \rho b_o\omega/\mu)$ with b_o and μ being the porosity coefficient and dynamic viscosity. The limiting case $b_o \to 0$ corresponds to the impermeable plate and $b_o \to \infty$ means that the plate is infinitely porous so that there is no obstruction in the fluid domain. The new dimensionless porosity parameter b used in the present numerical examples is defined as:

$$b = \frac{2\pi\sigma}{k_1} = \frac{2\pi\rho\omega b_o}{k_1\mu}. \tag{2.7}$$

By means of the eigenfunction expansion method, the fluid domain is divided into two regions, as shown in figure 1(*a*). Region (I) is defined by $x \leqslant -a$, $-h < y < 0$, and region (II) by $-a < x \leqslant 0$, $-h < y < 0$. The velocity potential in each fluid region satisfying the modified Helmholtz equation and boundary conditions (2.2)–(2.6), can

be written as follows:

$$\phi^{(1)} = -\frac{igA}{\omega}\left\{e^{-\alpha_{10}(x+a)} f_{10}(y), + \sum_{n=0}^{\infty} a_n e^{\alpha_{1n}(x+a)} f_{1n}(y)\right\}, \tag{2.8}$$

$$\phi^{(2)} = -\frac{igA}{\omega}\sum_{n=0}^{\infty} b_n \cos\alpha_{2n}x \; f_{2n}(y), \tag{2.9}$$

where A is the wave amplitude and

$$\alpha_{1n} = \begin{cases} -ik_1\cos\theta & (n=0) \\ \sqrt{k_1^2\sin^2\theta + k_{1n}^2} & (n \geqslant 1), \end{cases} \tag{2.10}$$

$$\alpha_{2n} = \sqrt{k_{2n}^2 - k_1^2\sin^2\theta} \qquad (n \geqslant 0), \tag{2.11}$$

The eigenfunctions $f_{1n}(y)$ are given by

$$f_{1n}(y) = \begin{cases} \dfrac{\cosh k_1(y+h)}{\cosh k_1 h} & (n=0), \\ \dfrac{\cos k_{1n}(y+h)}{\cos k_{1n}h} & (n \geqslant 1). \end{cases} \tag{2.12}$$

The eigenvalues k_{1n} are the solutions of the following equations

$$\begin{cases} k_1 \tanh k_1 h = \dfrac{\omega^2}{g} & (n=0), \\ k_{1n}\tan k_{1n}h = -\dfrac{\omega^2}{g} & (n \geqslant 1). \end{cases} \tag{2.13}$$

The eigenfunctions $f_{2n}(y)$ and eigenvalues k_{2n} in region (II) are the actual solutions of the following boundary-value problem of a function $\tilde{f}$ with parameter κ:

$$\begin{gathered} \frac{d^2\tilde{f}}{dy^2} - \kappa^2\tilde{f} = 0, \\ \frac{d\tilde{f}}{dy} - \nu\tilde{f} = 0 \quad \text{on} \quad y = 0, \\ \left.\frac{d\tilde{f}}{dy}\right|_{y=-d+0} = \left.\frac{d\tilde{f}}{dy}\right|_{y=-d-0} = i\sigma(\tilde{f}|_{y=-d-0} - \tilde{f}|_{y=-d+0}), \\ \frac{d\tilde{f}}{dy} = 0 \quad \text{on} \quad y = -h, \end{gathered} \tag{2.14}$$

for the upper complex plane of κ and $0 < \sigma < \infty$. Then, the following complex dispersion relation should be satisfied:

$$\kappa\sinh\kappa(h-d)(\nu\cosh\kappa d - \kappa\sinh\kappa d) = i\sigma(\nu\cosh\kappa h - \kappa\sinh\kappa h). \tag{2.15}$$

The real and imaginary parts of (2.15) have to be respectively zero. With initial guesses of all the roots, the ordinary nonlinear equation can be solved easily by using the Newton–Raphson iteration method. The infinite number of discrete solutions satisfying (2.15) are eigenvalues k_{2n}. The resulting eigenfunctions $f_{2n}(y)$ are

$$f_{2n}(y) = \begin{cases} \sinh k_{2n}(h-d)(k_{2n}\cosh k_{2n}y + \nu\sinh k_{2n}y) & (-d \leqslant y \leqslant 0), \\ (\nu\cosh k_{2n}d - k_{2n}\sinh k_{2n}d)\cosh k_{2n}(y+h) & (-h \leqslant y \leqslant -d). \end{cases} \tag{2.16}$$

By straightforward integration using (2.16), it can be shown that the eigenfunctions satisfy $\int_{-h}^{0} f_{2n}(y) f_{2m}(y)\,\mathrm{d}y = 0,\ m \neq n$.

The unknown coefficients a_n, $b_n (n = 0, 1, 2, \ldots)$ can then be determined by invoking the continuity of potential and horizontal velocity at $x = -a$. The continuity of ϕ at $x = -a$ requires that

$$f_{10}(y) + \sum_{n=0}^{\infty} a_n f_{1n}(y) = \sum_{n=0}^{\infty} b_n \cos \alpha_{2n} a\ f_{2n}(y) \quad (-h \leqslant y \leqslant 0). \tag{2.17}$$

Multiplying (2.17) by $f_{2m}(y)$ and integrating with respect to y over $[-h, 0]$, we obtain

$$b_m \cos \alpha_{2m} a\, N_m^{(2)} = C_{m0} + \sum_{n=0}^{\infty} a_n C_{mn}, \tag{2.18}$$

where

$$\begin{aligned} C_{mn} &= \int_{-h}^{0} f_{1n}(y) f_{2m}(y)\,\mathrm{d}y \\ \int_{-h}^{0} f_{2n}(y) f_{2m}(y)\,\mathrm{d}y &= \begin{cases} N_m^{(2)} & (m = n) \\ 0 & (m \neq n). \end{cases} \end{aligned} \tag{2.19}$$

On the other hand, the continuity of $\partial\phi/\partial x$ at $x = -a$ gives

$$-\alpha_{10} f_{10}(y) + \sum_{n=0}^{\infty} \alpha_{1n} a_n f_{1n}(y) = \sum_{n=0}^{\infty} \alpha_{2n} b_n \sin \alpha_{2n} a\ f_{2n}(y) \quad (-h \leqslant y \leqslant 0). \tag{2.20}$$

Multiplying both sides of (2.20) by $f_{1m}(y)$ and integrating with respect to y from $-h$ to 0, we obtain

$$-\alpha_{10} N_0^{(1)} + \alpha_{10} a_0 N_0^{(1)} = \sum_{n=0}^{\infty} \alpha_{2n} b_n \sin \alpha_{2n} a C_{n0} \quad (m = 0), \tag{2.21a}$$

$$\alpha_{1m} a_m N_m^{(1)} = \sum_{n=0}^{\infty} \alpha_{2n} b_n \sin \alpha_{2n} a\, C_{nm} \quad (m \neq 0), \tag{2.21b}$$

where

$$\int_{-h}^{0} f_{1n}(y) f_{1m}(y)\,\mathrm{d}y = \begin{cases} N_m^{(1)} & (m = n), \\ 0 & (m \neq n). \end{cases}$$

The final matrix equation for a_m can then be obtained by substituting (2.18) into (2.21) after truncating m and n to N:

$$\begin{aligned} a_0 + \sum_{k=0}^{N} \frac{F_{0k}}{\alpha_{10} N_0^{(1)}} a_k &= \left(1 - \frac{F_{00}}{\alpha_{10} N_0^{(1)}}\right) \quad (m = 0), \\ a_m + \sum_{k=0}^{N} \frac{F_{mk}}{\alpha_{1m} N_m^{(1)}} a_k &= -\frac{F_{m0}}{\alpha_{1m} N_m^{(1)}} \qquad (m = 1, 2, 3, \ldots, N), \end{aligned} \tag{2.22}$$

where

$$F_{mk} = -\sum_{n=0}^{N} \frac{\alpha_{2n} \tan \alpha_{2n} a\, C_{nm}\, C_{nk}}{N_n^{(2)}}. \tag{2.23}$$

By solving the above simultaneous algebraic equations, the unknown constants a_n can be determined. Subsequently, another unknown constants b_n can be obtained from (2.18).

Finally, the reflection coefficients and the dimensionless free surface profile above a porous plate can be determined from

$$R_f = |a_0|, \quad \eta/A = \sum_{n=0}^{N} b_n \cos \alpha_{2n} x \; f_{2n}(0). \tag{2.24}$$

The vertical hydrodynamic force on the horizontal porous plate can be calculated from

$$F = -\mathrm{i}\rho\omega \int_{-a}^{0} \left[\phi^{(2)}(x, -d_-) - \phi^{(2)}(x, -d_+)\right] \mathrm{d}x. \tag{2.25}$$

3. Boundary-element numerical method

In this section, a numerical method based on a boundary integral equation (e.g. Brebbia & Dominguez 1992) is developed to confirm the MEE solutions derived in the preceding section. It can also be straightforwardly generalized to the problem of multiple inclined porous plates. The fluid domain is decomposed into two regions, inner and outer regions, as shown in figure 1(*b*). The outer solution is expressed by the expansion of eigenfunctions satisfying the modified Helmholz equation as well as free-surface, bottom and radiation boundary conditions. The inner domain is divided into two sub-regions (figure 1*b*). For the case of dual porous plates, the inner domain is divided into three sub-regions. The inner solution in region I satisfies the boundary-value problem given by (2.2)–(2.4); on the other hand, the inner solution in region II satisfies the bottom condition (2.3), the body boundary condition (2.4), and wall condition (2.5). In addition, the inner solutions are to be matched to outer solutions at the respective matching boundaries. The velocity potential in the inner region can be obtained by applying Green's theorem with a Green function G. The resulting integral equation is given by

$$-\begin{pmatrix} \phi(x, y) \\ \frac{1}{2}\phi(x, y) \end{pmatrix} = \int_{\Gamma} \left(\phi \frac{\partial G}{\partial n} - G \frac{\partial \phi}{\partial n}\right) \mathrm{d}S \begin{pmatrix} \text{if } (x, y) \in \Omega \text{but not on } \Gamma \\ \text{if } (x, y) \text{ on } \Gamma \end{pmatrix} \tag{3.1}$$

where the Green function G is the fundamental solution satisfying $\nabla^2 G - k_1^2 \sin^2\theta G = -\delta\,(x - x_o)\delta(y - y_o)$, and given by

$$G(x, y; x_o, y_o) = \frac{1}{2\pi} K_0(k_1 \sin\theta\, r), \quad r = \sqrt{(x - x_o)^2 + (y - y_o)^2}, \tag{3.2}$$

where r is the distance between source point (x, y) and field point (x_0, y_0) and K_0 is the second-kind modified Bessel function of zeroth order. The normal derivative of G can also be obtained analytically in terms of K_1. In the two-dimensional case of normal incidence $\theta \to 0$, $K_0(k_1 \sin\theta r)$ approaches $-\ln r$, in which the logarithmic function can be used as a simple source. To convert the above integral equation to a matrix equation, the entire boundary of the inner region has to be discretized by N_T elements, and the values of ϕ and $\partial\phi/\partial n$ are assumed to be constant over each element. Using the simple source, the bottom topography of the inner region can be arbitrary. Substituting the boundary conditions of region I into (3.1), the following

equation is obtained

$$\sum \left(H^{ij} - \frac{\omega^2}{g} G^{ij} \right) \phi_j^{(1)}\big|_{\Gamma_F} + \sum H^{ij} \phi_j^{(1)}\big|_{\Gamma_-} + \sum H^{ij} \phi_j^{(1)}\big|_{\Gamma_{b1}} + \sum H^{ij} \phi_j^{(1)}\big|_{\Gamma_M} + \sum (H^{ij} - \mathrm{i}\sigma G^{ij}) \phi_j^{(1)}\big|_{\Gamma_S} + \sum \mathrm{i}\sigma G^{ij} \phi_j^{(2)}|_{\Gamma_S} + \sum H^{ij} \phi_j^{(1)}\big|_{\Gamma_W} = \sum G^{ij} \frac{\partial \phi_j^{(1)}}{\partial n}\bigg|_{\Gamma_-} + \sum G^{ij} \frac{\partial \phi_j^{(1)}}{\partial n}\bigg|_{\Gamma_M}, \tag{3.3}$$

where Γ_F, Γ_-, Γ_{b1}, Γ_M, Γ_S, Γ_W are the free surface, matching boundary I (with outer region), bottom surface, matching boundary II (with region II), porous plate surface, and vertical wall, respectively. The influence coefficients H and G are defined by

$$H^{ij} = \int_{\Gamma_j} \frac{\partial G}{\partial n} \mathrm{d}S, \quad G^{ij} = \int_{\Gamma_j} G \, \mathrm{d}S. \tag{3.4}$$

Similarly, substituting the boundary conditions of region II into (3.1), we obtain

$$\sum \mathrm{i}\sigma G^{ij} \phi_j^{(1)}\big|_{\Gamma_S} + \sum (H^{ij} - \mathrm{i}\sigma G^{ij}) \phi_j^{(2)}\big|_{\Gamma_S} + \sum H^{ij} \phi_j^{(2)}\big|_{\Gamma_M} + \sum H^{ij} \phi_j^{(2)}\big|_{\Gamma_{b2}} + \sum H^{ij} \phi_j^{(2)}\bigg|_{\Gamma_W} = \sum G^{ij} \frac{\partial \phi_j^{(2)}}{\partial n}\bigg|_{\Gamma_M}. \tag{3.5}$$

At the matching boundary Γ_M, the pressure and normal velocity must be continuous

$$\frac{\partial \bar{\phi}}{\partial n} = \frac{\partial \phi^{(1)}}{\partial n} = -\frac{\partial \phi^{(2)}}{\partial n}, \quad \bar{\phi} = \phi^{(1)} = \phi^{(2)} \quad \text{at} \quad \Gamma_M, \tag{3.6}$$

where the upper bar means the value newly defined at the matching boundary Γ_M.

Substituting (3.6) into (3.3) and (3.5), we obtain the following matrix equations.

$$\left([H] - \frac{\omega^2}{g} [G] \right) [\phi^{(1)}]|_{\Gamma_F} + [H][\phi^{(1)}]|_{\Gamma_-} + [H][\phi^{(1)}]|_{\Gamma_{b1}} + [H][\bar{\phi}]|_{\Gamma_M} + ([H] - \mathrm{i}\sigma [G])[\phi^{(1)}]|_{\Gamma_S} + \mathrm{i}\sigma [G][\phi^{(2)}]|_{\Gamma_S} + [H][\phi^{(1)}]|_{\Gamma_W} - [G] \left[\frac{\partial \bar{\phi}}{\partial n} \right] \Bigg|_{\Gamma_M} - [G] \left[\frac{\partial \phi^{(1)}}{\partial n} \right] \Bigg|_{\Gamma_-} = 0, \tag{3.7}$$

$$\mathrm{i}\sigma [G][\phi^{(1)}]|_{\Gamma_S} + [H][\bar{\phi}]|_{\Gamma_M} + ([H] - \mathrm{i}\sigma [G])[\phi^{(2)}]|_{\Gamma_S} + [H][\phi^{(2)}]|_{\Gamma_{b2}} + [H][\phi^{(2)}]|_{\Gamma_W} + [G] \left[\frac{\partial \bar{\phi}}{\partial n} \right] \Bigg|_{\Gamma_M} = 0. \tag{3.8}$$

By applying another matching condition (continuity of pressure and normal velocity) between the outer solution (eigenfunction-expansion solution satisfying the radiation condition as described in § 2) and the inner solution in region I at Γ_-, a final matrix equation can be derived and the unknown coefficients of the outer solution can be determined.

4. Small- and full-scale experiments

In order to validate the theory and numerical procedure developed in the preceding sections, we conducted a series of experiments in a two-dimensional wave tank (20 m

long, 0.6 m wide, and 1.0 m deep) located at MOERI. The glass-walled wave tank is equipped with a dry-back, piston type wavemaker capable of producing regular and irregular waves. The wave elevation was measured with resistance-type wave gauges having an accuracy of ± 0.1 cm. Four probes for decomposing incident and reflected waves are installed at positions of 4.0 m, 4.4 m, 4.67 m, and 4.864 m from the front of the porous plates, respectively. The estimation of the reflection coefficient was based on a least-squares technique applied to the measurements from four probes (Mansard & Funke 1980). Regular waves were generated by user-defined time-voltage inputs to the wavemaker. The wave frequency range used in our experiments was from 0.5 to 1.4 Hz. The porous plate model was made of a punched steel plate with six different porosities ($P = 0.0567$, 0.0740, 0.1008, 0.2267, 0.3, 0.4031). The length, width, and thickness of the porous plates were 60 cm, 60 cm and 1.6 mm. The thickness was determined in order to maintain rigidity while resisting the hydrodynamic force of (2.25). The porous plates were attached with the desired angle to four vertical steel frames clamped to the tank bottom. Table 1 summarizes the principal specifications of the models and wave characteristics used in our experiments. The details of the perforated plates are given in table 2.

Prior to the final design and fabrication of MOERI's wave absorber, a series of full-scale tests were also conducted in the square basin with prototype (length = 3 m, width = 8 m, thickness = 2.5 mm) horizontal and inclined porous plates in front of a rigid wall. Similar to the two-dimensional experiment, four probes (capacitance-type with accuracy ± 0.3 cm and sampling rate = 20 Hz) at 3 m, 3.65 m, 4.24 m and 4.92 m from the plate front were used to decompose the incident and reflected waves. Regular waves of steepness 0.02–0.04 and frequency range 0.28 to 2.0 Hz were generated by the 88-segment piston-type multi-directional wavemaker whose vertical position can be adjusted. The inclined plates were attached to vertical frames positioned with 2 m spacing. The test was conducted at the water depth 1.5 m with submergence depth $d = 15$ cm, inclination angle $\beta = 5^\circ$, 10°, and plate porosity $P = 0.1$. Small- and large-scale tests were continuously observed to make sure that the wave absorption was not due to wave breaking.

5. Numerical/experimental results and discussions

The MEE solutions and the independently developed BEM results are compared for cross-checking. First, the convergence of the MEE solutions with the number of eigenfunctions N is shown in table 3 for the case $a/h = 1.0$, $b = 5.0$, $d/h = 0.2$, $\theta = 0^\circ$. It is seen that the convergence is rapid for various values of non-dimensional wavelength and $N = 20$ is selected for the ensuing calculations.

Next, the MEE solutions are compared in figure 2 with the BEM-based numerical results. For the BEM result, 350 total elements with 100 elements on the free surface were used. The two solutions are in good agreement. As the plate-submergence depth decreases, reflection coefficients are reduced significantly for a wide range of wavelengths, which means that shallower porous plates more effectively interact with surface waves to lessen wave reflection.

In figure 3, the MEE solutions are compared with the two-dimensional tank experimental results. The x-axis is the non-dimensional wavelength and y-axis is the reflection coefficients for two different porous parameters. For comparison, the porous parameter was empirically determined from the experiments with various types of porous plates. The porous parameter b may depend on the porosity and shape/size of holes. We found from our experiments that if the circular holes are sufficiently small and arrayed uniformly, the porous parameter depends mainly on the porosity

(*a*)	Exp. 1 (horizontal)	Exp. 2 (inclined)		Exp. 3 (dual)	
Number of plates	1	1		2	
Water depth (cm)	60	60		60	
Length of porous plate (cm)	60	60		60	
Width of porous plate (cm)	60	60		60	
Submergence depth (cm)	1.5	Front	Rear	Upper	Lower
		5		1.5	11.5
		8	0		22.0
		17			
Porosity	0.0567 0.0740 0.1008 0.2267 0.3000 0.4031	0.1008		0.1008	
Inclined angle (deg.)	0	4.7 7.6 16.5		0	
Wave frequency range (Hz)	0.5–1.4	0.5–1.4		0.5–1.4	
Wave steepness (H/λ)	0.0051–0.0133	0.0051–0.0133		0.0051–0.0133	

(*b*)	Exp. 4 (prototype)		Exp. 5 (MOERI)	
Number of plates	Inclined (1)		Inclined (5) Vertical (6)	
Length of porous plate (m)	3		3 (inclined) 3 (vertical)	
Submergence depth (cm)	Front	Rear	Front	Rear
	15	15	59	0
	26	0		
	52	0		
Water depth (m)	1.5		1.21 1.29 1.36 1.40	
Porosity	0.1		0.1	
Inclined angle (deg.)	0 5 10		11.3	
Wave frequency range (Hz)	0.28–2.0		0.28–2.0	
Wave steepness (H/λ)	0.02–0.04		0.02–0.04	

TABLE 1. (*a*) Experimental conditions in a two-dimensional wave tank. (*b*) Experimental conditions in a square basin.

rather than on the size of holes. Then, the empirical relationship between the porous parameter b and the plate porosity P was determined from the least-squares fitting technique as follows:

$$S = \sum_{i=1}^{M} [R_f(f_i, P) - \bar{R}_f(f_i, b)]^2,$$

P	Diameter of hole (mm)	Spacing of adjacent holes (mm)
0.0567	2	8
0.0740	2	7
0.1008	2	6
	4	12
	8	24
	12	36
0.2267	2	4
	5	10
0.3000	4	7
0.4031	4	6

TABLE 2. Specification of porous plates used in a two-dimensional wave tank.

Truncated Numbers N	Reflection coefficient R_f			
	$a/\lambda = 0.2$	$a/\lambda = 0.4$	$a/\lambda = 0.6$	$a/\lambda = 0.8$
5	0.2490	0.2153	0.2289	0.3893
10	0.2481	0.2157	0.2259	0.3903
15	0.2482	0.2177	0.2245	0.3917
20	0.2480	0.2170	0.2240	0.3918
25	0.2480	0.2171	0.2238	0.3918

TABLE 3. Convergence of R_f for different values of N.

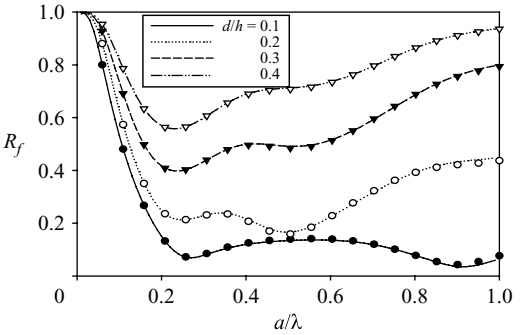

FIGURE 2. Reflection coefficient of an horizontal porous plate as a function of non-dimensional wavelength a/λ and submergence depth for $a/h = 1.0$, $b = 5.0$, $\theta = 0^\circ$ (lines are for MEE solutions and symbol are for BEM solutions).

where f_i are wave frequencies and M is the number of wave frequencies. $R_f(f_i, P)$ are the measured reflection coefficients for a given porosity P and $\bar{R}_f(f_i, b)$ are the calculated reflection coefficients. The porosity parameter corresponding to the given porosity is then determined by minimizing the squared error S. The fitted curve (see figure 4) is the linear function that can be expressed by $b = 57.63P - 0.9717$. The developed empirical formula is valid for thin punched plates with circular holes arrayed uniformly.

All the lines in figure 3 are the MEE solutions (reflection coefficient against plate-length to wavelength ratio for submergence depth $= 2.5\,\%$ of water depth) produced

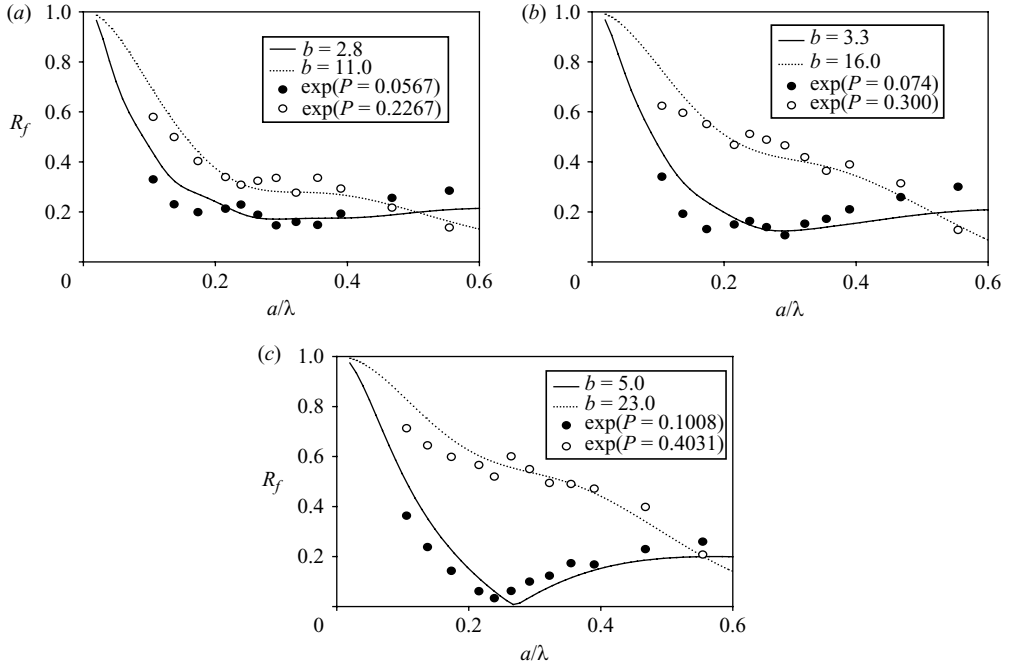

FIGURE 3. Comparison of theoretical reflection coefficients with experimental results as a function of a/λ for $d/h = 0.025$, $a/h = 1.0$, $\theta = 0°$.

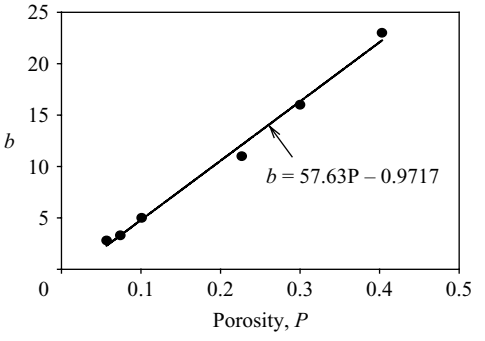

FIGURE 4. Regression line between the porous parameter and the porosity.

with the empirically determined porous parameter. The six curves cover a wide range of six different porosities $b = 2.8$–23 (table 4). In general, the cases of relatively smaller porosity ($b = 2.8$–5.0 or $P = 0.057$–0.1) perform better than those of larger porosity ($b = 11$–23 or $P = 0.23$–0.40) as wave absorber. When $b = 5$, reflection coefficients become less than 10 % when the wave length is 3–5 times the plate length. The theoretically predicted curves correlate well with the experimental results for such a wide range of plate porosities.

All the curves of figure 3 were obtained for a given plate submergence depth. To further validate the developed theory and assess the effects of plate submergence depth d, additional experiments for $d = 2$, 5, and 10 cm were also conducted. For

Porosity (P)	Porous parameter (b)
0.0567	2.8
0.0740	3.3
0.1008	5.0
0.2267	11.0
0.3000	16.0
0.4031	23.0

TABLE 4. Porous parameter corresponding to given porosities.

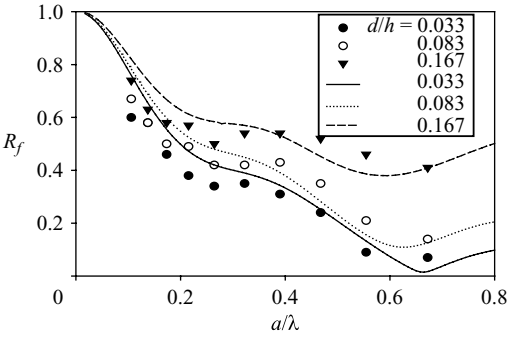

FIGURE 5. Comparison of analytic and experimental results for a horizontal punched plate with a vertical wall as a function of a/λ and submergence depth ($P = 0.28$, $a/h = 1.0$, $\theta = 0°$).

this experiment, $P = 0.28$ ($b = 15.16$) was selected for plate porosity. Both theoretical predictions and experimental results are plotted in figure 5 and they are generally in good agreement. It is seen both in theory and experiment that reflection coefficients increase with plate submergence depth (see also figure 2). Therefore, to be an effective wave absorber, the porous horizontal plate should be placed closed to the free surface.

So far, the porous parameter b has been a function of the porosity P only. Then, what will happen if the porosity remains the same, while the hole size changes? To answer this question, a series of experiments have been conducted with four different hole diameters (2, 4, 8 and 12 mm) and spacing (6, 12, 24 and 36 mm) while keeping the same porosity $P = 0.1008$ ($b = 5.0$). The experimental results are plotted in figure 6 along with a theoretical prediction with $b = 5$. The figure shows how wave reflection varies with hole size under the same porosity. If the resulting wave reflection coefficients change much for different hole sizes, then the hole diameter should also be an additional independent parameter in the numerical modelling. It is found that the wave reflection coefficients are not sensitive to the change of hole diameter and show a consistent trend with narrow spread. They all agree well with the theoretical prediction with the single parameter $b = 5$.

To find the best design of a horizontal-plate-based wave absorber with the optimal values of porosity and submergence depth, extensive calculations have been conducted and two contour plots are produced in figure 7. Through the two contour plots, we can easily find the smallest wave reflection for a particular combination of plate length, submergence depth and porosity. It is seen that the reflection coefficient is maintained below 10 % in a wide range of $0.07 < P < 0.12$, $d/h < 0.15$ and $a/\lambda > 0.2$.

Next, we consider the performance of inclined porous plates as wave absorber. In figure 8, the BEM-based reflection coefficients are plotted as a function of a/λ for

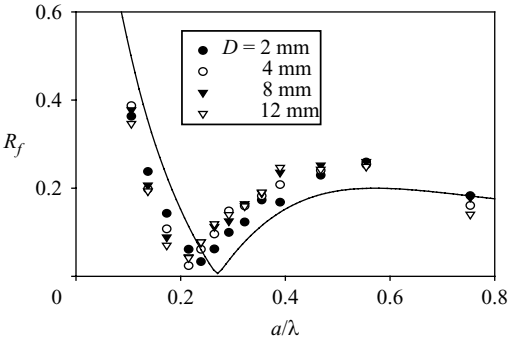

FIGURE 6. Comparison of analytic and experimental results for a horizontal punched plate with a vertical wall as a function of a/λ and hole size ($P = 0.1008$, $a/h = 1.0$, $d/h = 0.025$, $\theta = 0°$). ——— calculation.

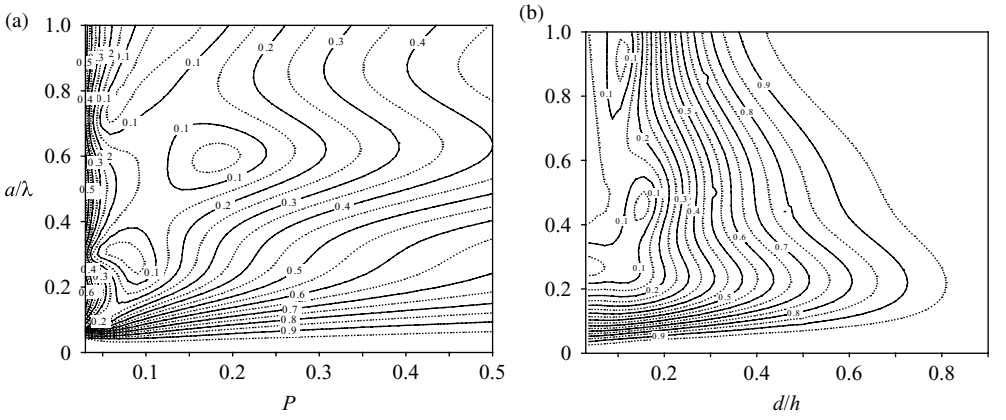

FIGURE 7. (*a*) Contour plots of reflection coefficients as a function of porosity (P) and a/λ for $d/h = 0.1$, $a/h = 1.0$, $\theta = 0°$. (*b*) Contour plots of reflection coefficients as a function of submergence depth (d/h) and a/λ for $P = 0.1$, $a/h = 1.0$, $\theta = 0°$

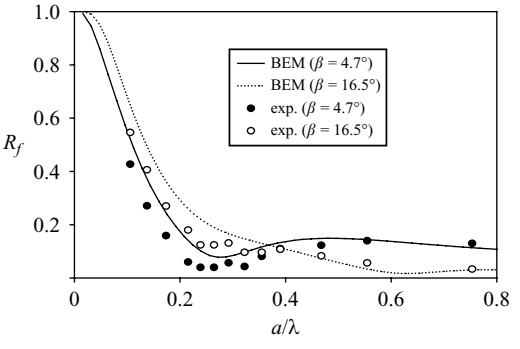

FIGURE 8. Comparison of numerical (BEM) and experimental results for an inclined porous plate with a vertical wall as a function of a/λ and inclined angles (β) for $P = 0.1008$, $a/h = 1.0$.

two different plate angles. The porosity is fixed at $0.1008(b = 5)$ and the plate-length to water-depth ratio $a/h = 1.0$. The BEM solutions are compared with experimental results. The rear of the plate is clamped to the vertical endwall at the mean water level and the front part is submerged at 5 and 17 cm, respectively. As the inclination

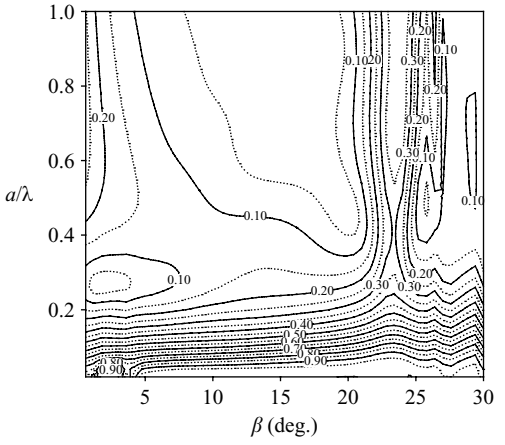

FIGURE 9. Contour plots of reflection coefficients as a function of inclined angles (β) and a/λ for $P = 0.1$, $a/h = 1.0$, $\theta = 0°$.

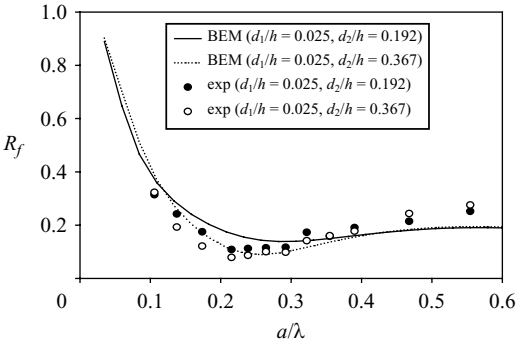

FIGURE 10. Comparison of numerical (BEM) and experimental results for dual porous plates with a vertical wall as a function of a/λ and submergence depth for $P = 0.1008$, $a/h = 1.0$, $\theta = 0°$.

angle increases, wave reflection is reduced in high-frequency region but increases in the range of $a/\lambda < 0.4$. Compared to the horizontal-plate case of the same porosity (figure 6), the overall wave-absorption performance is improved by imposing small inclination angles. The measured values generally follow the trend of the computed curve, which again validates the present theoretical prediction with an empirically determined porous parameter.

More extensive calculations are carried out in order to plot wave reflection coefficients as functions of both non-dimensional wavelengths and inclination angles (figure 9). It is seen that the optimal range of inclination angle is $10° < \beta < 20°$. If the inclination angle is greater than 20°, the performance of wave-absorption becomes worse. It is also seen that wave reflection is not reduced much in the long- wave regime $a/\lambda < 0.2$, regardless of inclination angles.

Figure 10 shows the BEM solutions together with the experimental results for the dual horizontal porous plates ($P = 0.1008$). The upper plate is fixed at $d = 1.5$ cm, while two different submergence depths, 11.5 cm and 22 cm, are used for the lower plate to assess the effect of spacing. The figure shows no significant difference between the

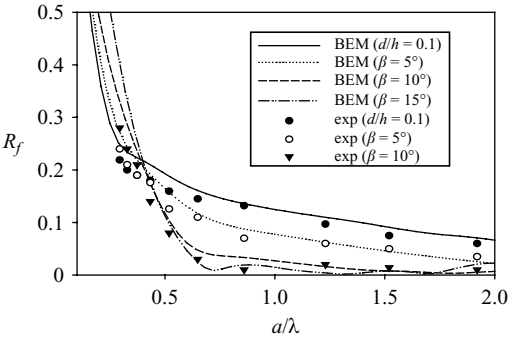

FIGURE 11. Comparison of numerical (BEM) and experimental results in a square basin for a submerged porous plate as a function of a/λ and inclined angle for $P = 0.1$, $a/h = 2.0$, $\theta = 0°$.

two. When compared with the upper-plate-only case (figure 6), there is no appreciable improvement in the performance of the wave absorption by adding the lower plate. The observation implies that the role of the lower plate in wave absorption is relatively minor compared to that of the upper plate.

Based on the two-dimensional experimental results and numerical predictions, we found that the optimal range of porosity and inclination angle are $0.07 < P < 0.12$ and $10° < \beta < 20°$ when $a/\lambda > 0.2$. It was also found that the addition of a lower porous plate does not appreciably improve the overall wave absorption efficiency. From this finding, the prototype wave absorber using an inclined porous plate was designed and installed at MOERI's square basin. For final verification of the developed concept and to assess possible scale effects, a full-scale test with an inclined porous plate ($P = 0.1$) was conducted in the square basin. The plate length was 3 m and the width was 8 m. The water depth was fixed at 1.5 m ($a/h = 2$). The plate length was chosen in order to cover a wavelength of up to 15 m considering the optimal condition $a/\lambda > 0.2$. The experimental condition is summarized in table 1(b) (Exp. 4). The full-scale tests were carried out for three different inclination angles (horizontal at $d = 15$ cm and inclined with $\beta = 5°$, 10°) and the corresponding theoretical predictions are also given (figure 11). The experimental results can be reproduced well by the developed theory even for the present full-scale case. As was confirmed in our previous study, the inclined porous plates show better efficiency than the horizontal one and the performance of the 10° case is the best. For reference, another theoretical curve for $\beta = 15°$ is also plotted in figure 11 to show that the case $\beta = 10°$ is already very good and there is no appreciable improvement by further increasing the inclination angle. The resultant wave forces (in normal direction) on each plate are compared for different inclination angles (figure 12a). The wave loading monotonically decreases as inclination angle increases in the range considered. It is also interesting to compare wave-induced forces for different plate porosities. The results corresponding to $b = 2.8$, 5 and 16 are plotted in figure 12(b). As can be intuitively expected, the wave loading monotonically decreases as plates become more porous.

Since the present theory and numerical method are developed to cover arbitrary incident wave headings, the wave absorption efficiency for oblique incident waves is also numerically tested. Figure 13 shows the predicted sensitivity of wave-absorption efficiency against incident wave angles. This kind of result is important since the designed inclined-plate wave absorber will be used for the multi-directional wave basin. It is seen that the wave absorption efficiency for oblique waves (up to 45°) is

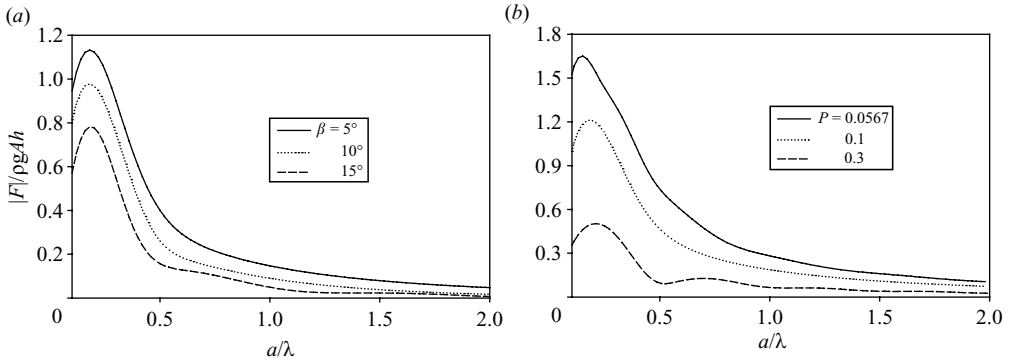

FIGURE 12. Hydrodynamic loading on (*a*) a submerged inclined porous plate as a function of a/λ and inclined angle for $P = 0.1$, $a/h = 2.0$, $\theta = 0°$, and (*b*) a submerged horizontal porous plate as a function of a/λ and porosity for $d/h = 0.1$, $a/h = 2.0$, $\theta = 0°$.

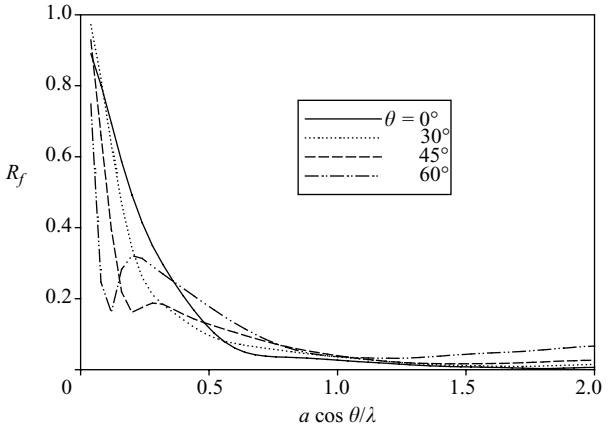

FIGURE 13. Reflection coefficient of a submerged porous plate as a function of $a\cos\theta/\lambda$ and incidence angle for $P = 0.1$, $a/h = 2.0$, $\beta = 10°$.

as good as that of a normal incidence angle. The performance in oblique waves can even be improved in the long-wave regime owing to smaller effective wavelengths in the direction of plate length.

Finally, figure 14 shows the design of the wave absorbing system for MOERI's square basin. To take advantage of the merits of both inclined and vertical types, the wave absorber consists of both types of porous plates. The vertical type is arrayed by six expanded metal sheets of three different porosities ($P = 0.6$ (front), 0.4, 0.2 (rear)) with 0.5 m spacing. The primary wave-energy is absorbed by the inclined porous plates with a length of 3 m, porosity 0.1 (diameter = 8 mm, spacing = 24 mm) and inclined angle 11.3°, which are attached to the first vertical plate. Five inclined porous plates are installed along the entire water depth ($h = 3.5$ m) to give a desirable performance at various water depths. Figure 15(*a*) shows the refection coefficients of MOERI's wave absorber at water depth $h = 1.36$ m for 12 wave periods in the range of 0.5–3.5 s. Two different wave slopes (H/λ) 0.02 and 0.04 are employed to assess the sensitivity to steeper/higher waves. At the given water depth, two inclined plates are involved and the rear part of the upper plate coincides with the free surface. Except for the longest wave $T = 3.5$ s, all the measured reflection coefficients are below 15 %.

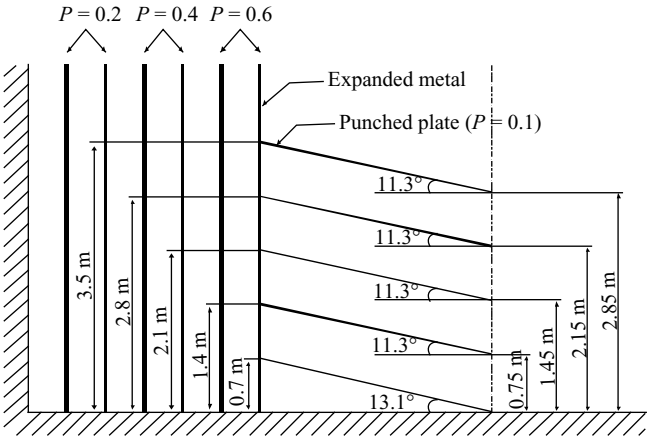

FIGURE 14. Side view of MOERI's inclined wave absorber.

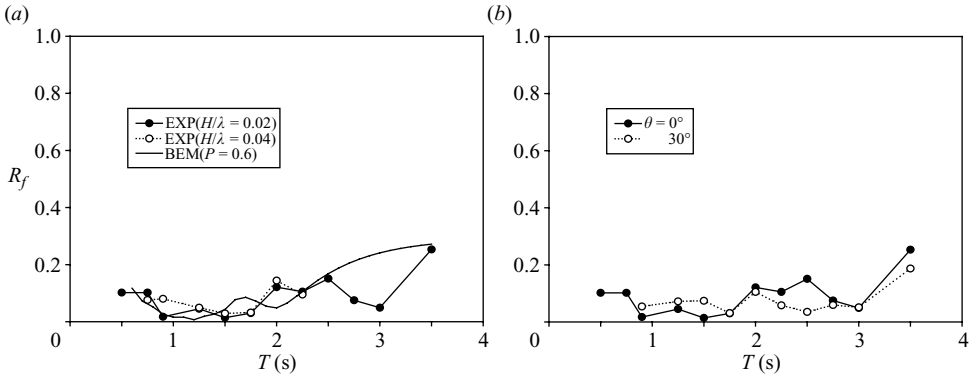

FIGURE 15. Reflection coefficient by MOERI's wave absorbing system (*a*) as a function of wave period and water steepness ($h = 1.36$ m, $\theta = 0°$), and (*b*) as a function of wave period and incidence angle ($h = 1.36$ m, $H/\lambda = 0.02$).

There is no appreciable change in absorption efficiency when doubling the wave height/slope, which implies that wave steepness (or nonlinearity) does not play an important role for overall performance within the range considered. In figure 15(*a*), the BEM solutions are also plotted for comparison. The BEM results are obtained by employing two inclined plates and one front vertical plate with porosity $P = 0.6$ (with rigid wall 1 m behind) at the same locations as in the MOERI design. For simplicity, only the front vertical porous plate is modelled instead of six arrays. As a result, four-domain solutions are matched at three porous plates. The numerical result correlates reasonably with the experimental results except for $T = 2.75$ s and 3 s, where the six arrays of vertical porous plates further dissipate the transmitted wave energy. Otherwise, the inclined plates play a major role in wave-energy absorption especially when $T < 2.5$ s. In figure 15(*b*) the change of reflection coefficients against incident wave headings is shown. As was already predicted by the developed theory (figure 13), the wave absorption efficiency is not sensitive to the change of wave-heading angle, thus is suitable for multi-directional wave basins.

6. Summary and conclusions

The wave absorption efficiency by using submerged horizontal or inclined porous plates was investigated in the context of two-dimensional linear potential theory, in which the viscous effects for porous thin plates are taken into consideration through Darcy's law. In § 2, MEE solutions for a submerged horizontal porous plate attached to a vertical wall were obtained by means of the eigenfunction expansion method. The MEE solutions were confirmed by the independently developed simple-source-based BEM solutions. Both MEE and BEM solutions included the case of oblique incident angles. The relationship between plate porosity and the porous parameter for numerical prediction was obtained from a curve-fitting technique using systematic experimental results. The analytical and BEM solutions with the empirical porous parameter are then compared with a series of experiments conducted in a two-dimensional wave tank. The small-scale test results correlated well with the predicted results.

Using the developed computer program, the wave absorption efficiency of a submerged porous plate was assessed for various wave and plate conditions, such as porosity, submergence depths, inclined angles, plate length and wavelengths. It was seen that an optimal combination of these design parameters existed for given plate length and water depth and it was not sensitive to the change of wave headings. As a result of the parametric study, plate-length 3 m, porosity 0.1, and inclined angle 11.3° are selected as an optimal design. To further verify the optimal selection of the design parameters, a series of full-scale experiments were also conducted in the MOERI's square wave basin. The full-scale experimental results were consistent with the predicted results as well as the small-scale test data. Finally, the same optimally selected inclined porous plate used for the full-scale testing was applied to the final design of the wave absorption system in MOERI's multi-directional wave basin. From the present study, it can be concluded that a properly designed submerged/inclined porous plate can be a very effective wave absorber and the optimal design parameters can be found through a comprehensive parametric study by using the developed numerical tool.

This work was supported by the research grant from the Chuongbong Academic Research Fund of Cheju National University in 2005

REFERENCES

Brebbia, C. A. & Dominguez, J. 1992 *Boundary Elements an Introductory Course*. McGraw-Hill.

Cho, I. H. & Kim, M. H. 1998 Interactions of a horizontal flexible membrane with oblique waves. *J. Fluid Mech.* **367**, 139–161.

Cho, I. H. & Kim, M. H. 1999 Wave deformation by a submerged flexible circular disk. *Appl. Ocean Res.* **21**, 263–280.

Chwang, A. T. 1983 A porous wavemaker theory. *J. Fluid Mech.* **132**, 395–406.

Chwang, A. T. & Wu, J. 1994 Wave scattering by submerged porous disk. *J. Waterway Port Coastal Ocean Engng* **120**, 2575–2587.

Evans, D. V. 1990 The use of porous screens as wave dampers in narrow wave tank. *J. Engng Maths* **24**, 203–212.

McIver, M. 1985 Diffraction of water waves by a moored, horizontal, flat plate. *J. Engng Maths* **19**, 297–320.

Mansard, E. P. D. & Funke, E. R. 1980 The measurement of incident and reflected spectra using a least squares methods. *Proc. Coastal Engng* 154–172.

Mei, C. C., Liu, P. L.-F. & Ippen, A. T. 1974 Quadratic loss and scattering of long waves. *J. Waterway Port Coastal Ocean Engng* **100**, 217–239.

Ouellet, Y. & Datta, I. 1986 A survey of wave absorbers. *J. Hydraul. Res.* **24**, 265–280.

Siew, P. F. & Hurley, D. G. 1977 Long surface waves incident on a submerged horizontal plate. *J. Fluid Mech.* **83**, 141–151.

Tuck, E. O. 1975 Matching problem involving flows through small holes. *Adv. Appl. Mech.* **15**, 89–158.

Twu, S. W. & Lin, D. T. 1991 On a highly effective wave absorber. *Coastal Engng* **15**, 389–405.

Wu, J. H., Wan, Z. & Fang, Y. 1998 Wave reflection by a vertical wall with a horizontal submerged porous plate. *J. Ocean Engng* **25**, 767–779.

Yip, T. L. & Chwang, A. T. 2000 Perforated wall breakwater with internal horizontal plate. *J. Engng Mech.* **126**, 533–538.

Yu, X. P. & Chwang, A. T. 1993 Analysis of wave scattering by submerged disk. *J. Engng Mech.* **119**, 1804–1817.

Yu, X. P. & Chwang, A. T. 2002 Functional performance of a submerged and essentially horizontal plate for offshore wave control: a review. *Coastal Engng J.* **44**, 127–147.